Table S1. Reaction conditions explored for optimizing Suzuki vs Heck cross-coupling reactions in with di-alkenyl dibromofluorene monomers. Solvent/base systems: **1)** 1:1 toluene:H_2O + Na_2CO_3; **2)** 1:1 THF/H_2O + KO_tBu + NaCl.

Monomer /method	Solvent + Base System	Temp. (°C)	Time (hr)	M_N	PDI	Fluorenes (DP)	Polymer Yield
xPF-11, microwave	1	110	2	--	--	--	0%
xPF-11, oil bath	1	100	48	--	--	2 (DP 1)	0%
xPF-5, oil bath (slow addition)	1	100	6	--	--	2 (DP 1)	0%
xPF-5, microwave	1	100	0.5	--	--	2 (DP 1)	0%
xPF-5, microwave	2	60	1	5300	1.71	16 (DP 8)	66%
xPF-5, microwave	2	60	1.5	9200	2.10	30 (DP 15)	84%
xPF-11, microwave	2	60	1.5	9400	2.42	24 (DP 12)	93%

Table S2. Summary of polymer size and physical properties of alkene/alkyl side-chain poly(fluorene)s both with and without fluorenone incorporation. Differences in T_g values can be attributed to the slight variation in molecular weights and dispersities between polymer samples.

Polymer	M_n (kg/mol)	Number Avg. Fluorene units per chain	$Đ$	T_g (°C)
xPF-5	8.4	26	2.6	108
xPF-11	9.4	23	2.5	45
xPF/O-5	9.4	30	2.9	99
xPF/O-11	7.9	20	2.6	46

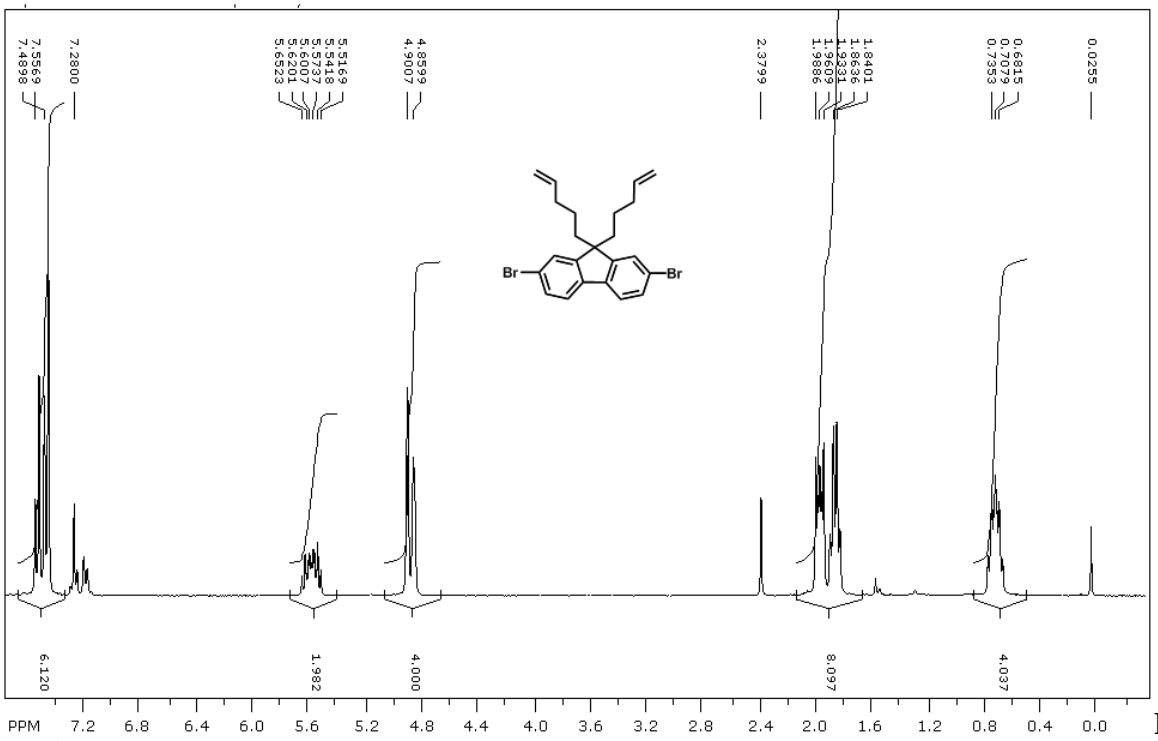

Figure S1. ^{1}H NMR spectra of 9,9-dipentenyl-2,7-dibromofluorene monomer. The aromatic impurities near 7.2 ppm are attributed to residual toluene from monomer synthesis.

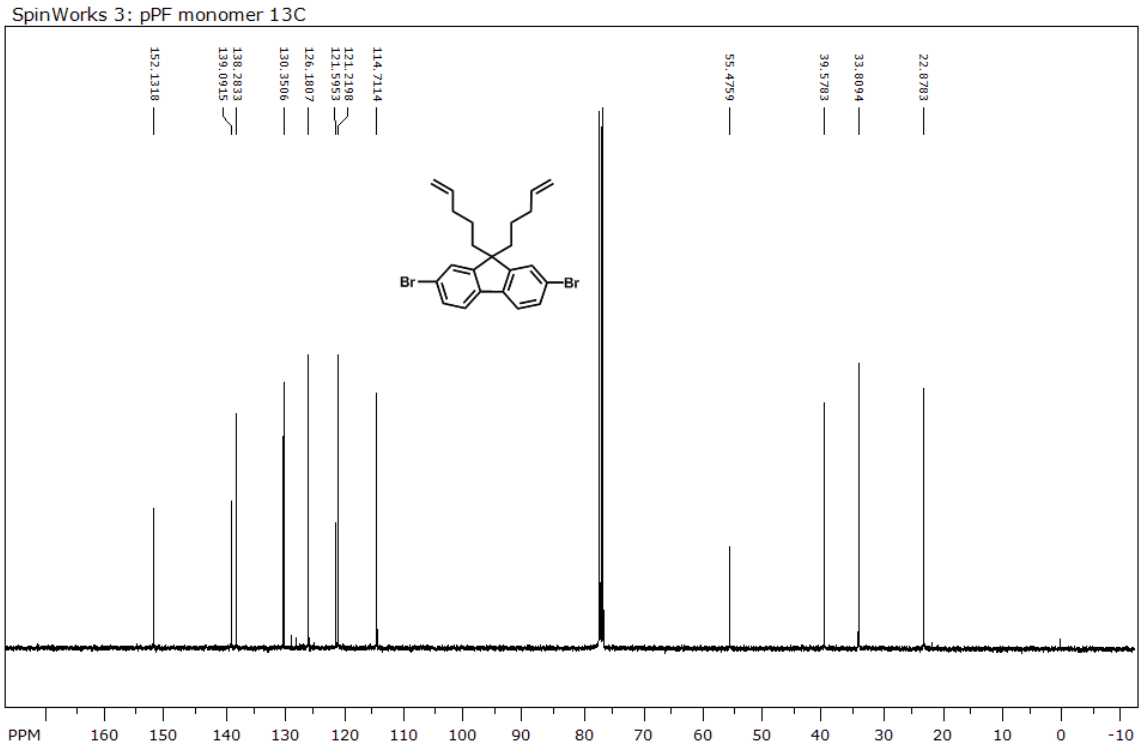

Figure S2. ^{13}C NMR spectra of 9,9-dipentenyl-2,7-dibromofluorene fluorene monomer. The aromatic impurities between 125-130 ppm are attributed to residual toluene from monomer synthesis.

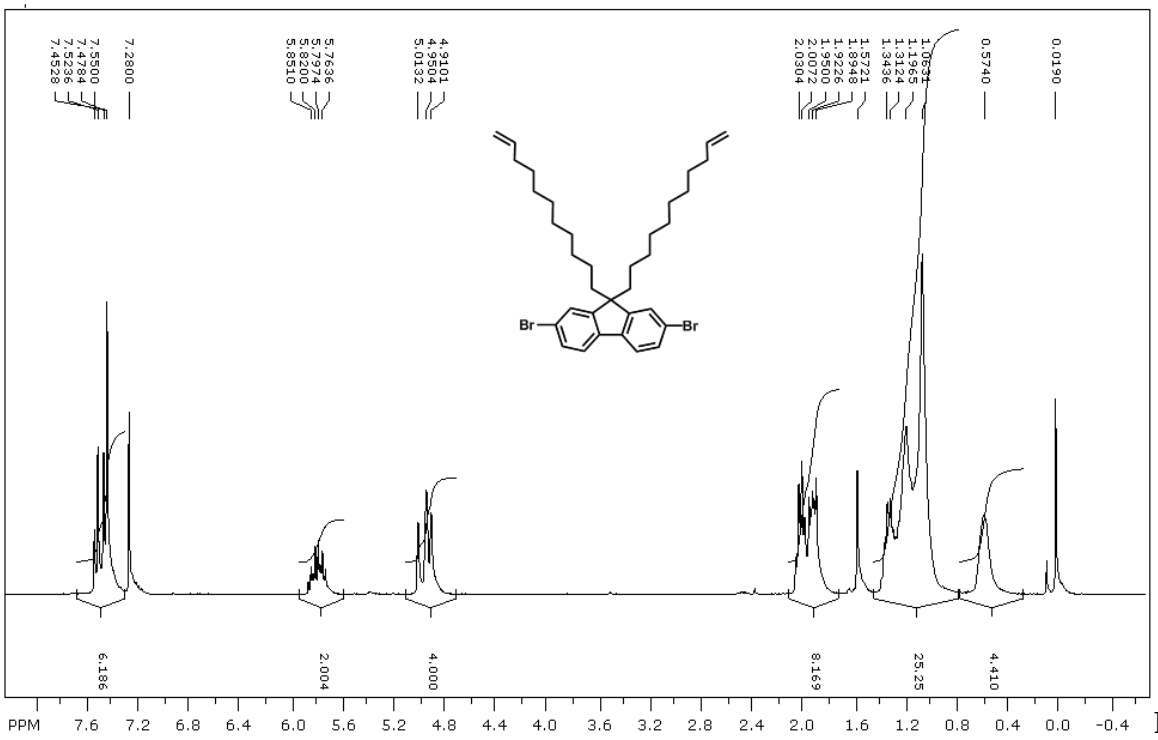

Figure S3. ^{1}H NMR spectra of 9,9-diundecenyl-2,7-dibromofluorene monomer.

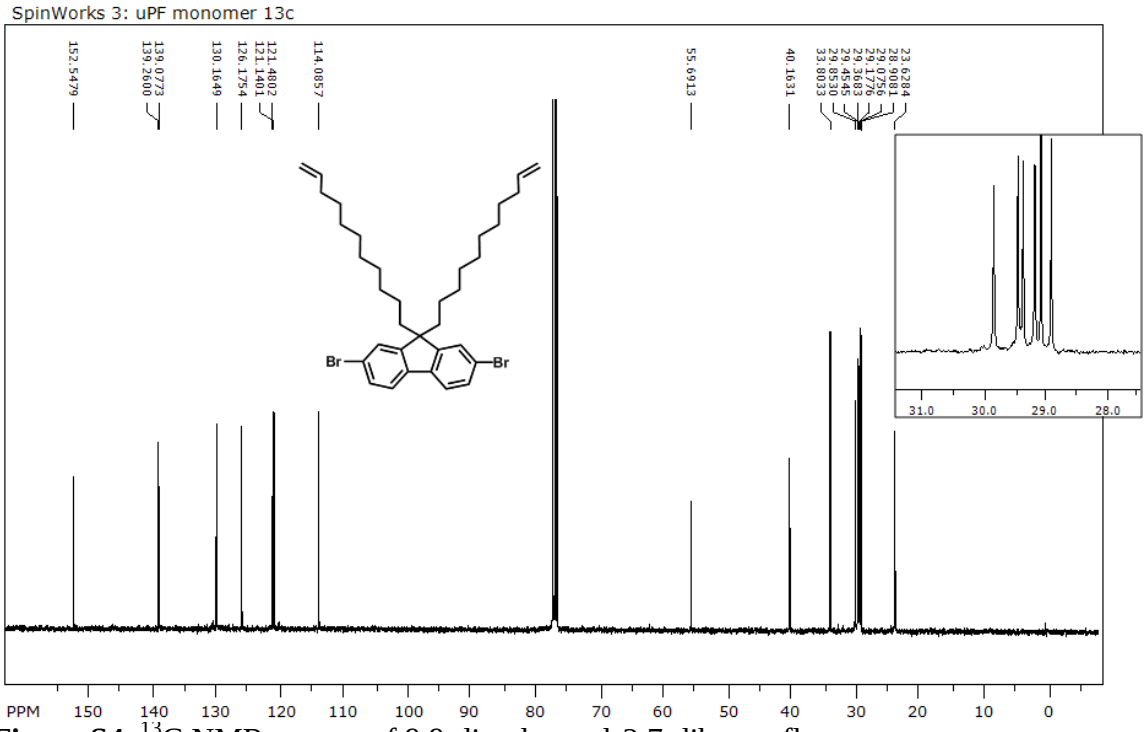

Figure S4. ^{13}C NMR spectra of 9,9-diundecenyl-2,7-dibromofluorene monomer.

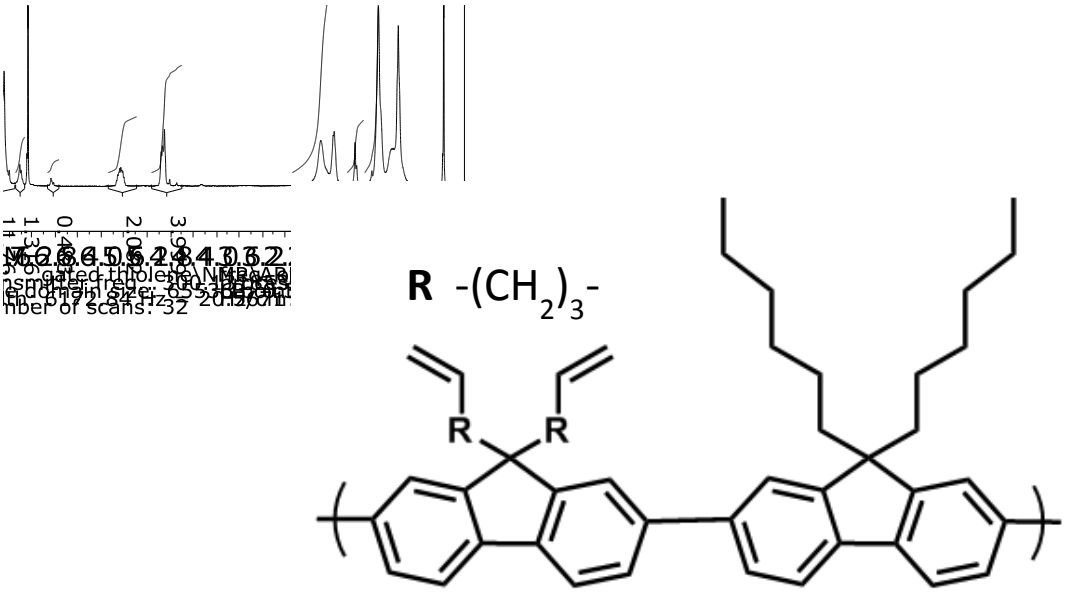

Figure S5. ^{1}H NMR spectra of xPF-5.

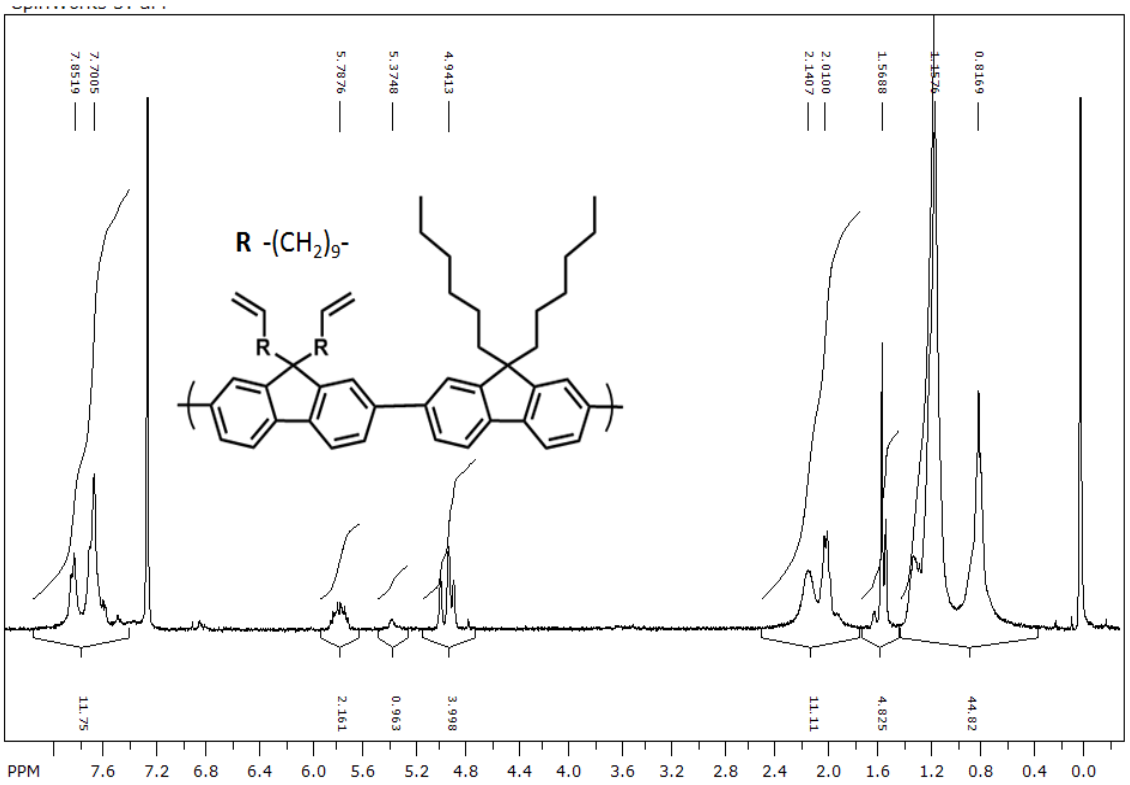

Figure S6. ^{1}H NMR spectra of xPF-11.

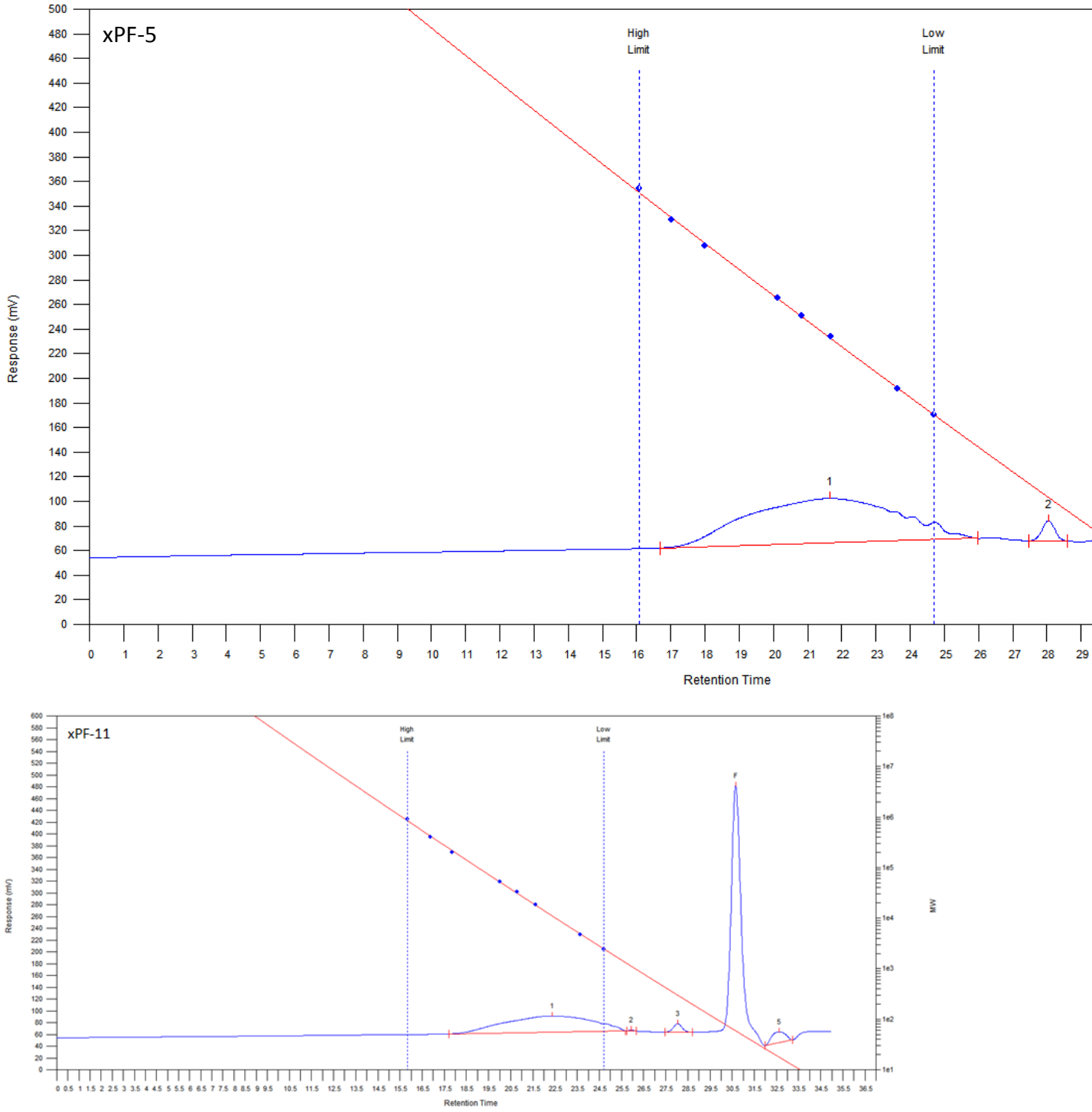

Figure S7. Gel permeation chromatography results for fluorenone-containing polymers xPF-5 and xPF-11 in tetrahydrofuran vs PS standards.

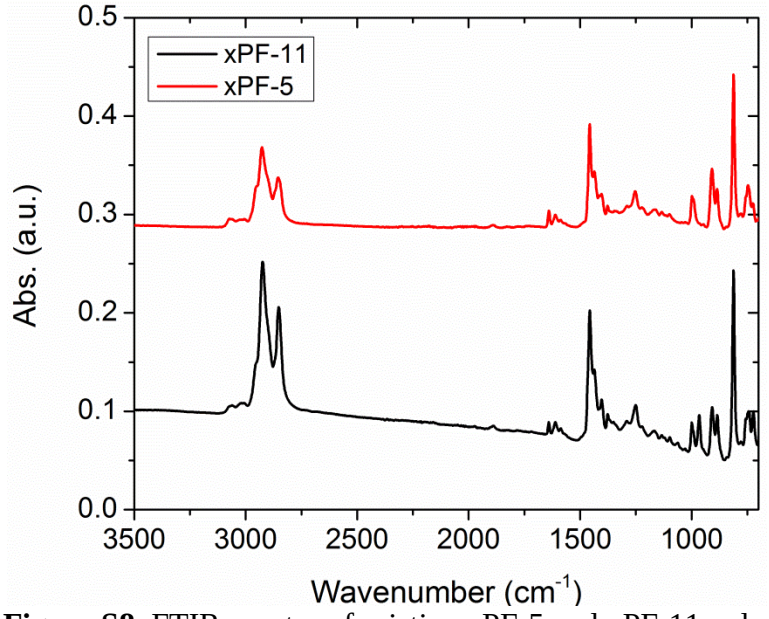

Figure S8. FTIR spectra of pristine xPF-5 and xPF-11 polymers without added thiol.

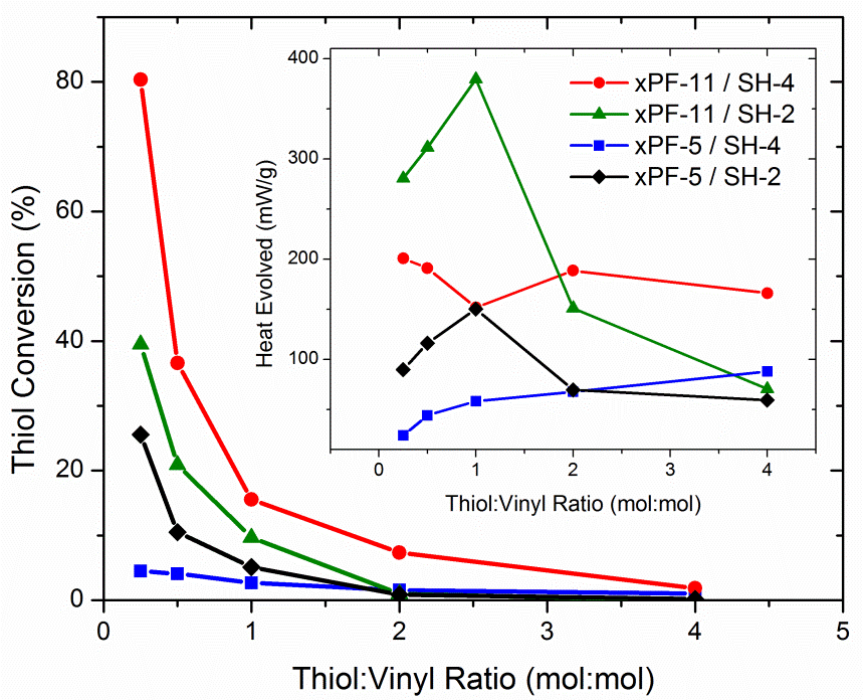

Figure S9. Extent of thiol conversion after 20 min. exposure to 1mW/cm^2 UV exposure as measured by heat evolved during photo curing. Inset shows total measured heat evolved during 20 min. of photo-curing (254 nm at 1mW/cm^2). Measured reaction enthalpies are considerably lower than theoretical thiol-ene reaction enthalpies for this system. This is likely due to required experimental constraints. Low sample masses (less than 3mg) and thin films were used to mimic device processing conditions, leading to very small reaction enthalpies, which are further complicated by environmental heating from the UV light source during photo calorimetry.

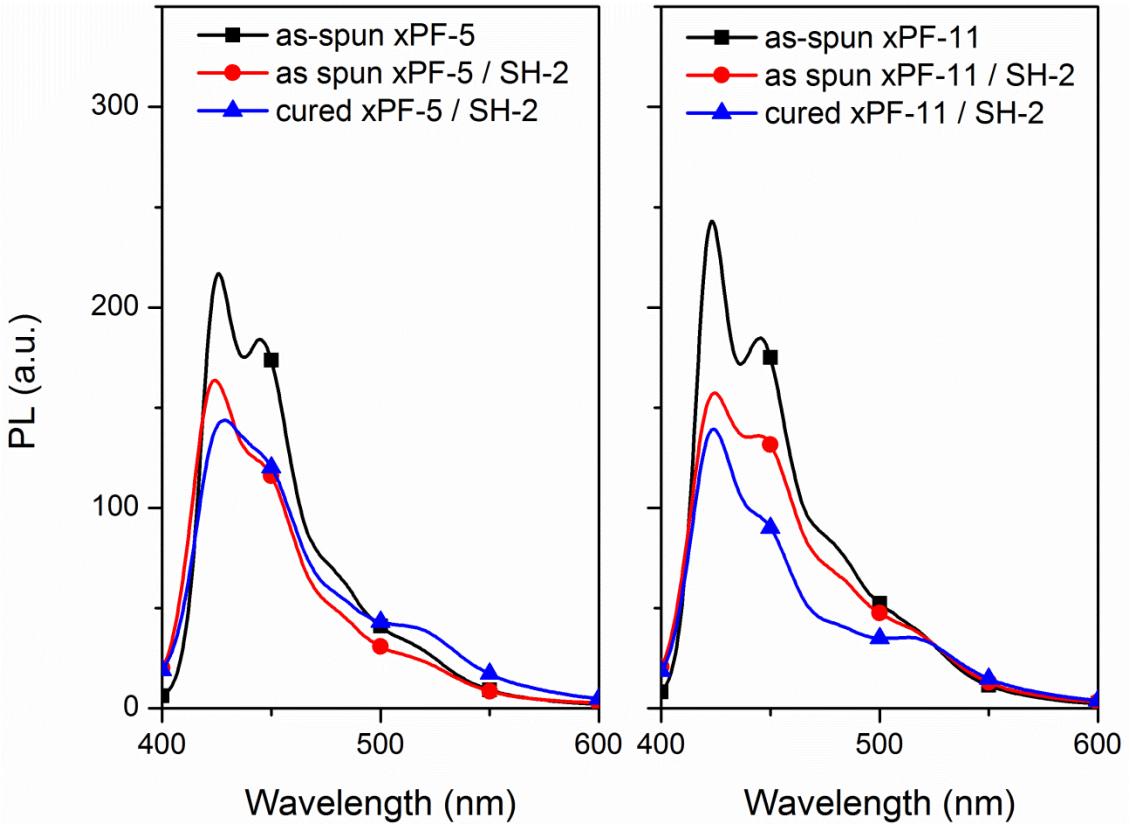

Figure S10. PL of xPF-5 and xPF-11 pristine thin films, as spun films with added thiol, and post-processed cured films. All thiol loadings are 1:1 molar ratio relative to vinyl groups.

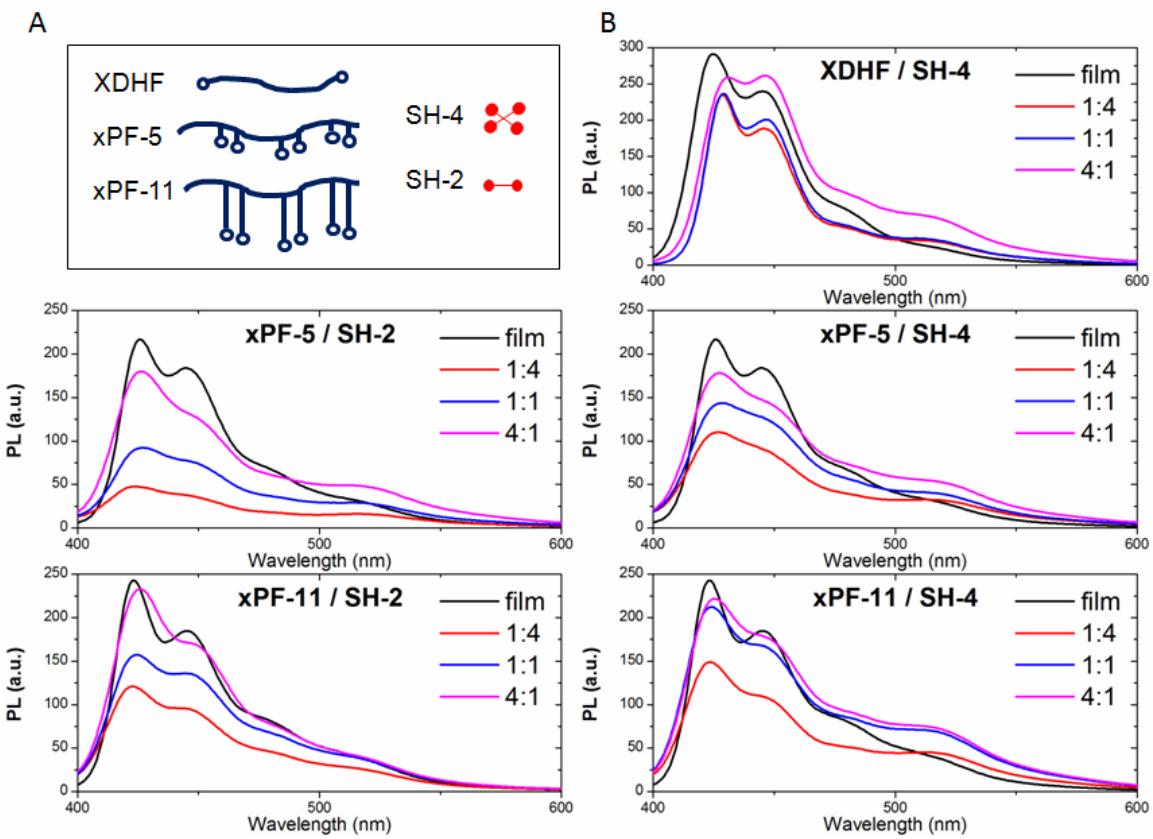

Figure S11. (A) Schematic cartoon representation of the salient details of each network component (end-chain vs short side-chain vs long side-chain reactivity, and thiol functionality). (B) Photoluminescence (PL) of poly(fluorene) films before and after network formation with dithiol SH-2 and tetrathiol SH-4 as a function of vinyl:thiol (mol:mol) loading, indicated in legends.

Supplemental Discussion: Immediately noticeable after curing is the decrease in PL intensity from the pristine film and the broadening of the vibronic features for the side-chain cross-linked polymers. In all cases, PL intensity increases overall as more thiol is added to polymer networks. Clearly excess free thiol does not quench photoemission. Next we compare the two variable side-chain lengths. The secondary 0-0 PL peak at 450 nm most markedly broadens after curing the shorter side-chain xPF-5 polymer. The longer side-chain xPF-11 cured networks show similar but less pronounced broadening of the secondary peak emission. The reduction of structural features in the xPF-5 networks' emission is suggestive of some distortion and inhomogeneity among the conjugated segments, likely as the shorter pentenyl side-chains pull on the polymer backbone during curing. xPF-11 also appears to show less reduction and change in PL than xPF-5, perhaps owing to the longer cross-linkable side chains which can flex through the curing network without distorting the conjugated packing.

The xPF-5 system shows greater sensitivity to cross-linker size and functionality as well. Curing with the shorter dithiol SH-2 leads to greater changes in PL intensity as a function of thiol loading compared to SH-4. By contrast, xPF-11 does not show this strong dependence. Again, this owes to the pentenyl side-chains of xPF-5 being shorter than the adjacent dihexyl groups on

the polymer backbone, and so network formation leads to more distortion in the interchain conjugated interactions than for xPF-11.

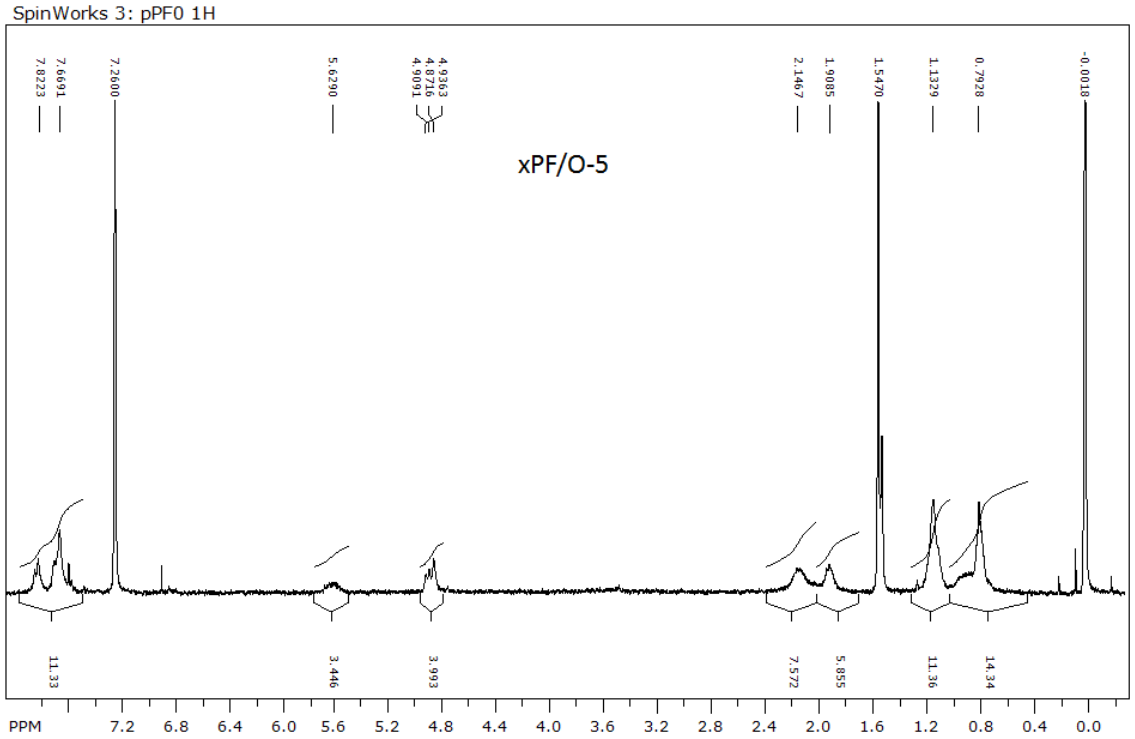

Figure S12. ^{1}H NMR spectra of fluorenone-containing xPF/O-5 polymer.

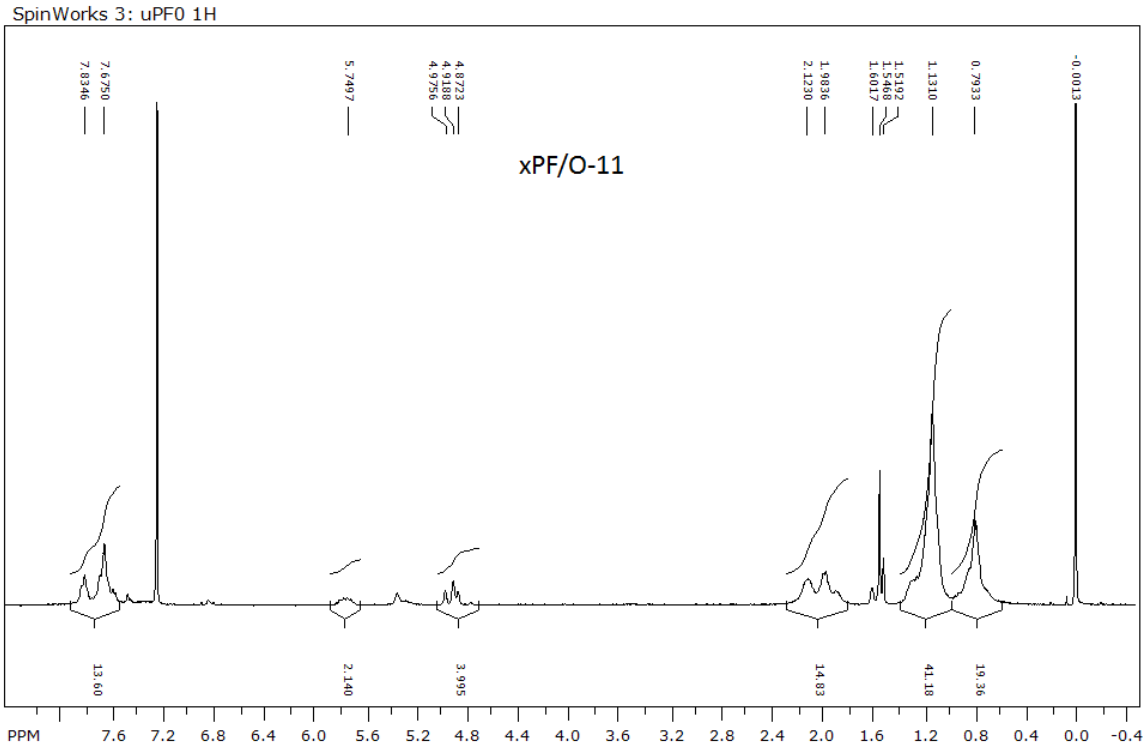

Figure S13. ^{1}H NMR spectra of fluorenone-containing xPF/O-11 polymer.

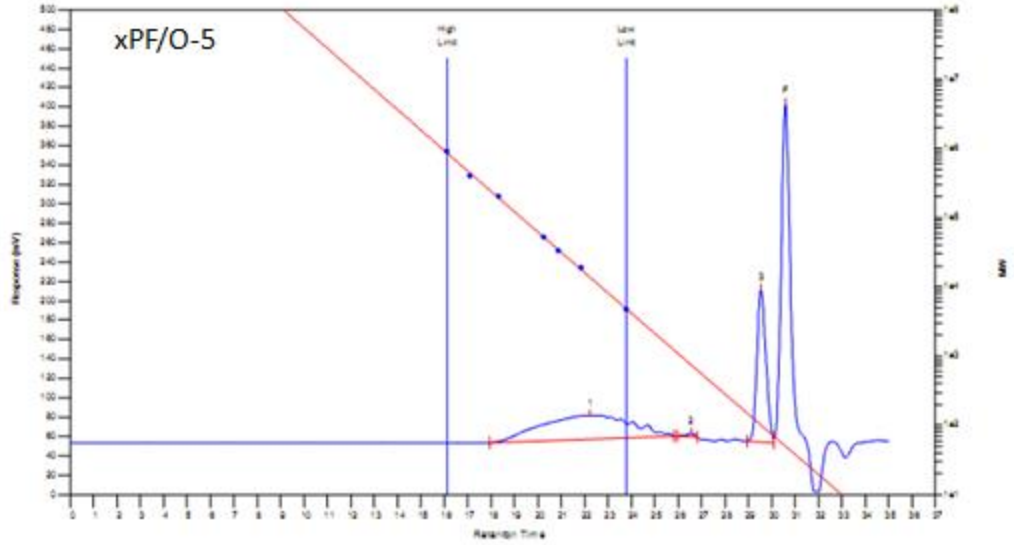

Peak No	Mp	Mn	Mw	Mz	Mz+1	Mv	PD
1	14032	9362	27708	61865	94112	23829	2.95982
2	736	787	799	812	826	797	1.01525
3	100	98	99	101	102	99	1.0102
4	0	0	0	0	0	0	0

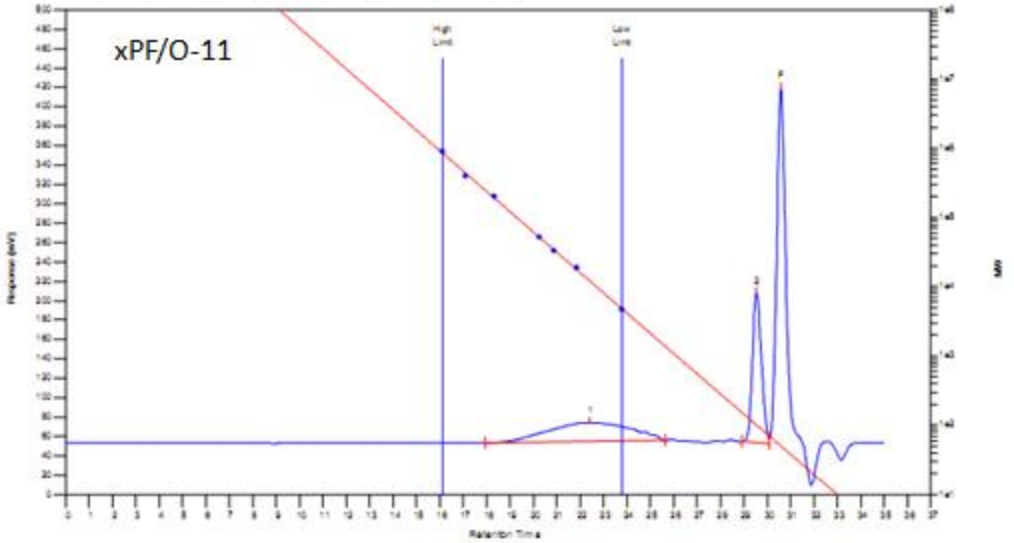

Peak No	Mp	Mn	Mw	Mz	Mz+1	Mv	PD
1	12971	7877	20476	45952	74496	17751	2.59947
2	100	98	99	100	102	99	1.0102
3	0	0	0	0	0	0	0

Figure S14. Gel permeation chromatography results for fluorenone-containing polymers xPF/O-5 and xPF/O-11 in tetrahydrofuran.

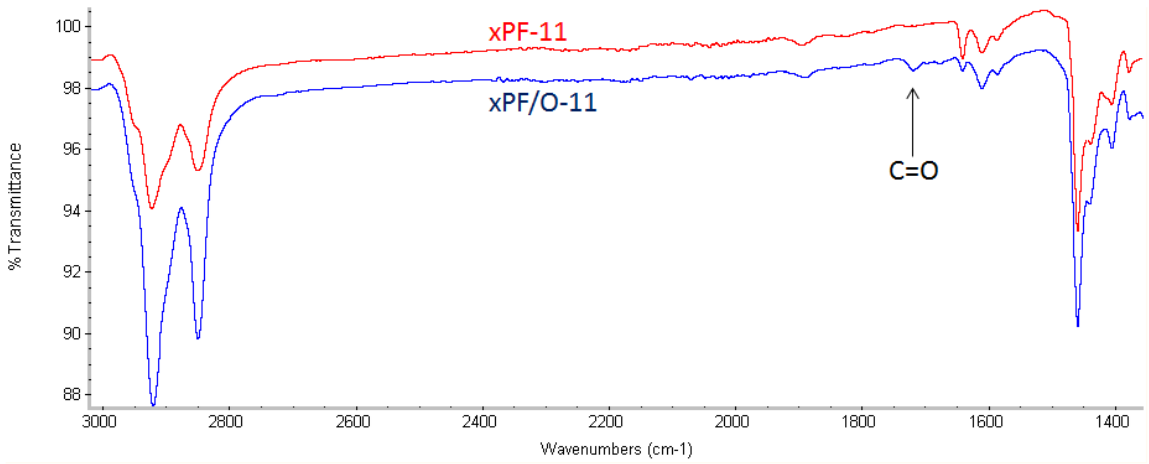

Figure S15. FTIR of pristine xPF-11 and fluorenone-containing xPF/O-11. Successful incorporation of fluorenone into the polymer is evidenced by the carbonyl peak at 1710 cm^{-1} seen only in the xPF/O-11 sample.

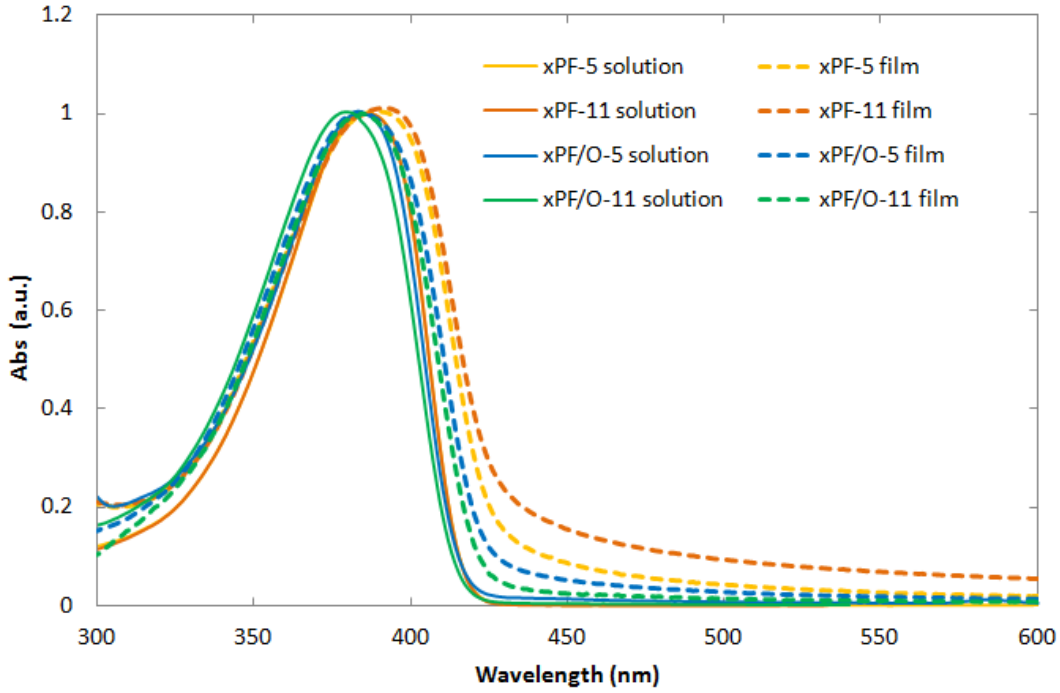

Figure S16. UV-vis absorption spectra of fluorenone-containing xPF/O-5 and xPF/O-11 compared to their fluorenone-free counterparts xPF-5 and xPF-11. Solution measurements were made in chloroform, and thin film measurements were made from films spin-coated from chloroform.

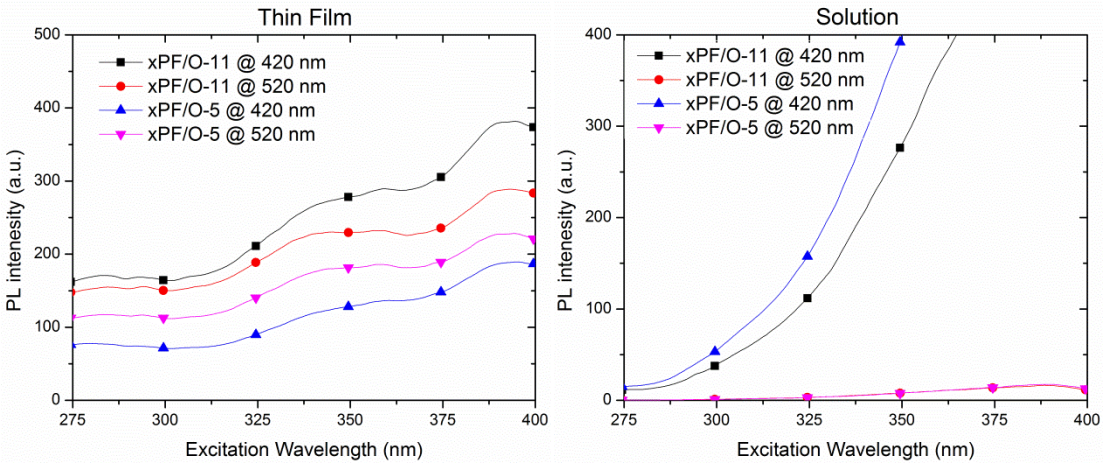

Figure S17. Excitation spectra of xPF/O-5 and xPF/O-11 polymers (in both solution and solid state) measured at 420 nm and 520 nm PL emission. The solution state spectra are plotted on a scale to emphasize the low-signal but clearly present 520 nm emission behavior.

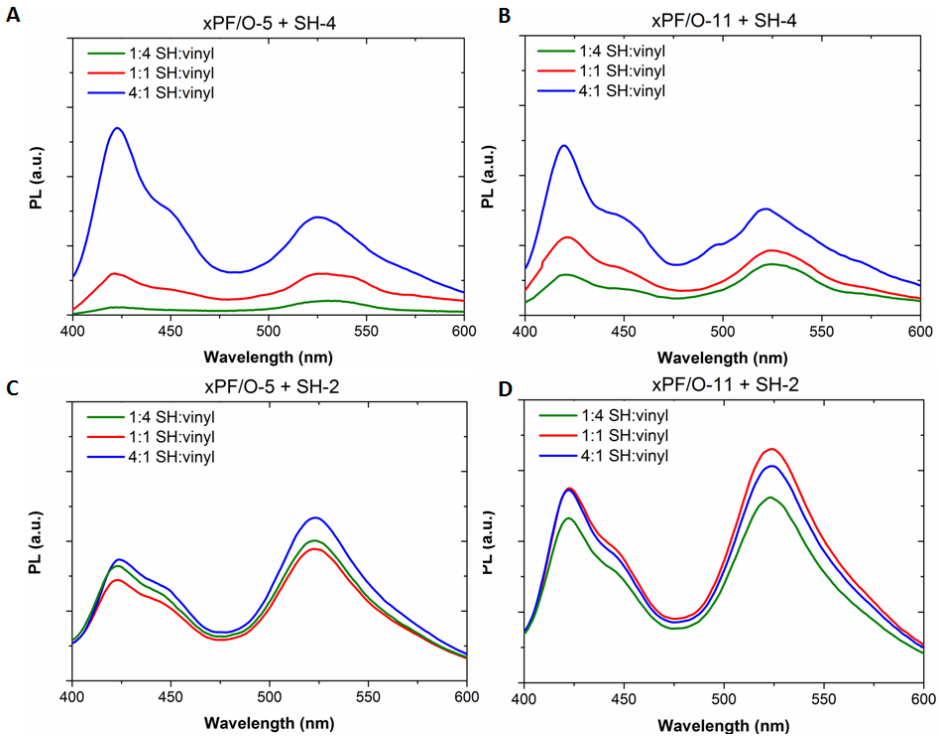

Figure S18. PL of cured xPF/O-5 and xPF/O-11 networks showing relative changes in PL intensity with curing and thiol functionality.

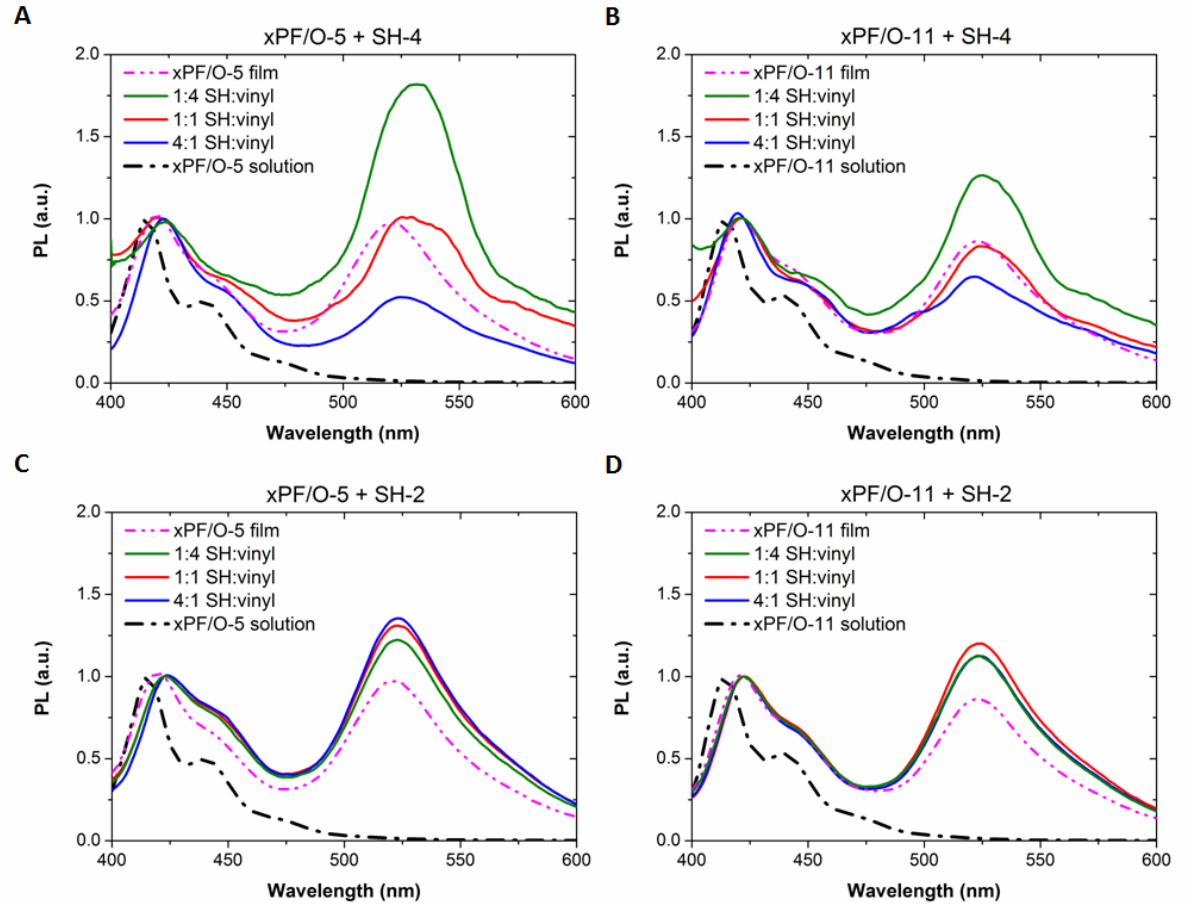

Figure S19. Photoluminescence (PL) of fluorenone-containing dipentenyl (xPF/O-5) and diundecenyl (xPF/O-11) cross-linked films as a function of thiol content for tetra-functional and di-functional thiol cross-linkers. PL spectra for thiol-free films and solutions of xPF/O-5 and xPF/O-11 are shown for comparison.

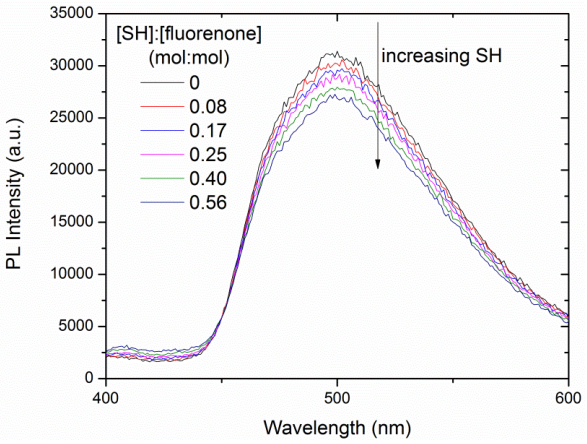

Figure S20. PL spectra of 2,7-dibromofluorenone monomer in toluene with increasing amounts of SH-4 added. Excitation wavelength is 320 nm.

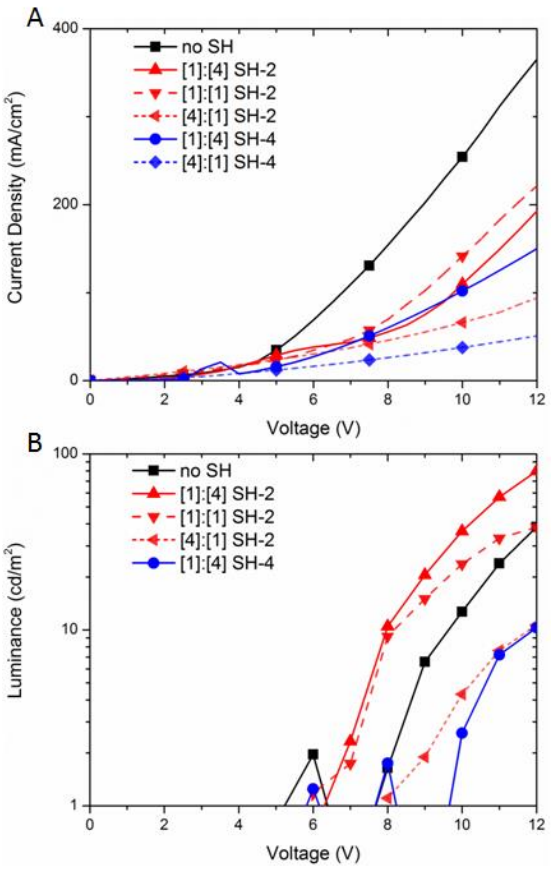

Figure S21. Current density-voltage (A) and luminance-voltage (B) output of best performing xPF-5 PLEDs.

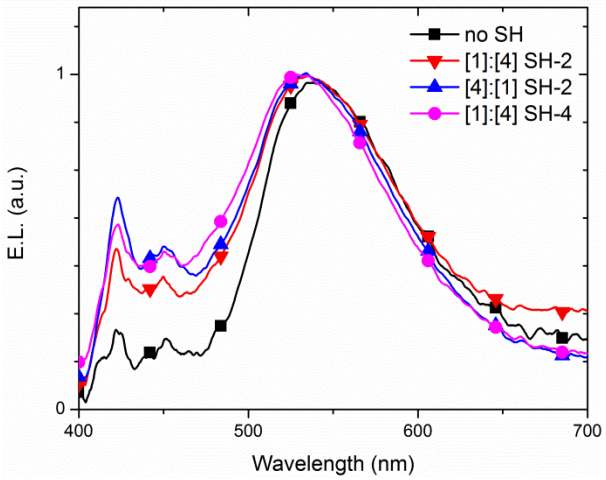

Figure S22. Electroluminescence (EL) spectra of xPF-5 PLEDs cross-linked with varying network architecture indicated in legend.

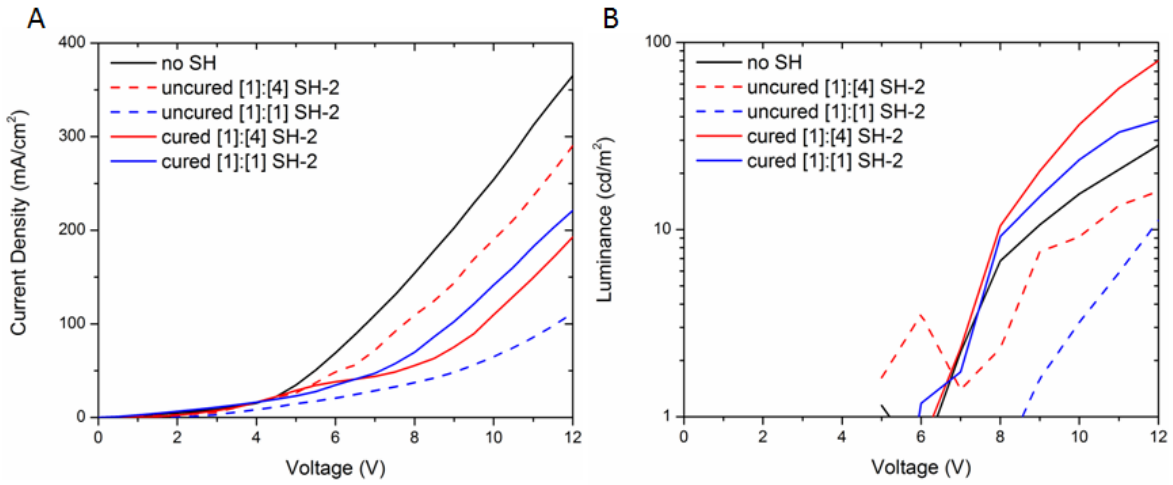

Figure S23. Comparisons of current density (A) and luminance (B) of PLEDs using an xPF-5 thin film without thiol, with added uncured thiol SH-2, and cross-linked with SH-2 as various active layers.

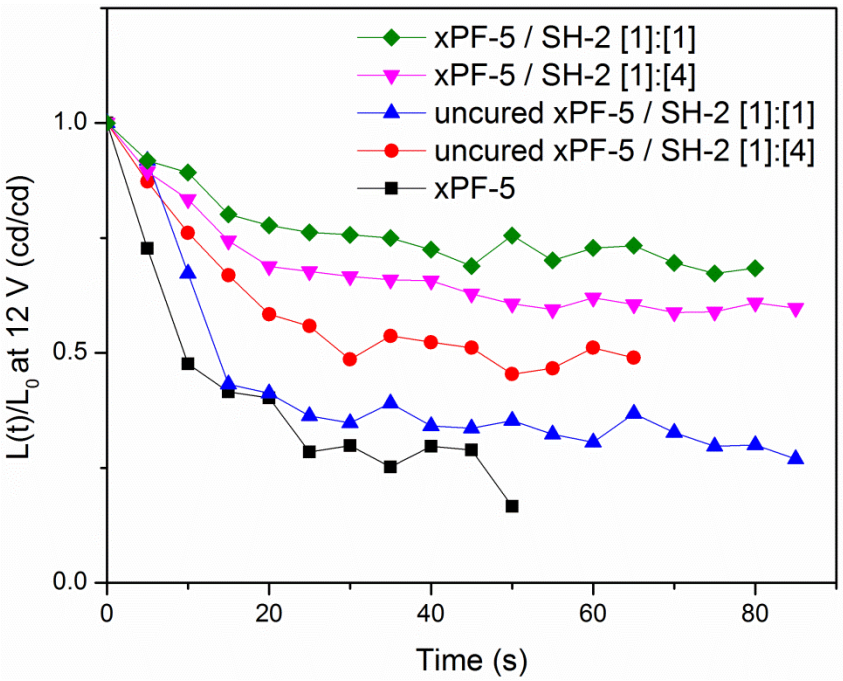

Figure S24. Atmospheric stability of xPF-5 PLEDs with various added and/or cured thiols. $L(t)/L_0$ y-axis represents the device brightness over time divided by the initial brightness when turned on at 12 V. Devices were continuously operated in air with no protective encapsulation.